Hydrol. Earth Syst. Sci. Discuss., 12, 8927–8976, 2015
www.hydrol-earth-syst-sci-discuss.net/12/8927/2015/
doi:10.5194/hessd-12-8927-2015

Hydrology and
Earth System
Sciences
Discussions
Open Access

Spatio-temporal variability of snow water equivalent in the extra-tropical Andes cordillera from a distributed energy balance modeling and remotely sensed snow cover

E. Cornwell[1], **N. P. Molotch**[2,3], **and J. McPhee**[1,4]

[1]Advanced Mining Technology Center, Facultad de Ciencias Físicas y Matemáticas, Universidad de Chile, Chile
[2]Department of Geography and Institute of Arctic and Alpine Research, University of Colorado, Boulder, USA
[3]Jet Propulsion Laboratory, California Institute of Technology, Pasadena, California, USA
[4]Departamento de Ingeniería Civil, Facultad de Ciencias Físicas y Matemáticas, Universidad de Chile, Chile

Received: 3 July 2015 – Accepted: 8 August 2015 – Published: 3 September 2015

Correspondence to: J. McPhee (jmcphee@u.uchile.cl)

Published by Copernicus Publications on behalf of the European Geosciences Union.

Abstract

Seasonal snow cover is the primary water resource precursor for human use and environmental sustain along the extratropical Andes Cordillera. Despite its importance, relatively little research has been devoted to understanding the properties, distribution and variability of this natural resource. This research provides high-resolution distributed estimates of end-of-winter and spring snow water equivalent over a 152 000 km^2 domain that includes the mountainous reaches of central Chile and Argentina. Remotely sensed fractional snow covered area and other relevant forcings are combined with extrapolated data from meteorological stations and a simplified physically-based energy balance model in order to obtain melt-season peak SWE. Estimates show an overall coefficient of determination R^2 of 0.61 compared to observations at 12 automatic snow water equivalent sensors distributed across the model domain, with R^2 values between 0.32 and 0.88. Regional estimates of peak SWE accumulation show differential patterns strongly modulated by elevation, latitude and position relative to the continental divide. Average peak SWE increases by nearly 500 mm for every 1000 m in elevation gain for the central and southern sub-regions of the model domain, but this effect is much less pronounced in the northern reaches. The 3000–4000 m a.s.l. elevation band is the most significant accumulation area for most of the northern and central reaches of the domain, although the 4000–5000 m a.s.l. band, despite a smaller contributing area, almost doubles the accumulation amounts estimated for the lower adjacent subdomain. Snow accumulation reaches an earlier peak in the western Andes, and the eastern side of the continental divide shows lower snow accumulation at all elevations except for the southern region represented by the Neuquén River Basin. The results presented here have the potential of informing applications such as seasonal forecast model assessment and improvement, regional climate model validation, as well as evaluation of observational networks and water resource infrastructure development.

1 Introduction

Accurately predicting the spatial and temporal distribution of snow water equivalent (SWE) in mountain environments remains a significant challenge for the scientific community and water resource practitioners around the world. The Andes Cordillera, a formidable mountain range that constitutes the backbone of the South American continent, remains one of the relatively least studied mountain environments due to its generally low accessibility and complex topography. The extratropical stretch of the Andes, extending south from approximately latitude 27° S, is a snow-dominated hydrological environment that provides key water resources for a majority of the population in Chile and Argentina. Until now, a very sparse network of snow courses and automated snow measuring stations (snow pillows) has been the only source of information about this key resource. In a context of sustained climate change characterized by warming trends and likely future precipitation reductions (Vera et al., 2006; Vicuña et al., 2011), it becomes ever more relevant to understand the past dynamics of the seasonal snowpack in order to validate predictive models of future snow-water resources. This research presents the first spatially and temporally explicit high-resolution SWE reconstruction over the snow-dominated extratropical Andes of central Chile and Argentina based on a physical representation of the snowpack energy balance (Kustas et al., 1994) and remotely sensed snow extent (Dietz et al., 2012) between years 2001 and 2014. A key advantage of the presented product is its independence from notoriously scarce and unreliable precipitation measurements at high elevations. Estimates of maximum SWE accumulation and depletion curves are obtained at 500 m resolution, coincident with the MODIS Fractional Snow Cover product MOD10A1 (Hall et al., 2002).

Patterns of hydroclimatic spatiotemporal variability in the extratropical Andes have been studied with increased intensity over the last couple of decades, as pressure for water resources has mounted while at the same time rapid changes in land use and climate have highlighted the societal need for increased understanding of water resource variability and trends under present and future climates. The vast majority of studies has relied on statistical analyses of instrumental records and regional climate models to present synoptic-scale summaries of precipitation (e.g. Aravena and Luckman, 2009; Falvey and Garreaud, 2007; Garreaud, 2009), temperature (Falvey and Garreaud, 2009), snow accumulation (Masiokas et al., 2006) and streamflow (Cortés et al., 2011; Núñez et al., 2013) variability. To the best of our knowledge, to date no high-resolution, large-scale distributed assessment of snow water equivalent, the most significant (per volume) water resource precursor in the region, is available.

The methods and assumptions required for SWE reconstruction have been tested and refined since they where first presented by Cline et al. (1998). Large-scale applications to mountain ranges have been presented in recent years. In the Sierra Nevada, Jepsen et al. (2012) compared SWE reconstructions to spatial regression from snow surveys ($R^2 = 0.79$), while Guan et al. (2013) obtained good correlation with snow sensors belonging to the SNOTEL network ($R^2 = 0.74$). In the Rocky Mountains, Jepsen et al. (2012) obtained an R2 value of 0.61 when comparing reconstructed SWE to spatial regression from snow surveys, and Molotch (2009) estimated SWE with a MAE = 23 % compared to intensive study areas. A useful discussion on the uncertainties of the SWE reconstruction method – albeit one based on temperature-index melt equations – was presented by Slater et al. (2013), who demonstrated that errors in forcing data are at least, if not more, important than snow covered area availability. The vast majority, if not all, of SWE reconstruction exercises have been developed in the Northern Hemisphere, under environmental conditions quite different from those predominant in the extratropical Andes Cordillera. Here, snow distribution and properties have been analyzed in a few local studies (e.g. Ayala et al., 2014; Cortés et al., 2014; Gascoin et al., 2013), but no large scale estimations at a relevant temporal and spatial resolution for hydrologic applications have been presented. In fact, the Andes of Chile and Argentina display near-ideal conditions for the estimation of peak and melt season SWE due to (1) the near absence of forest cover over a large fraction of the domain where snow accumulation is hydrologically significant, (2) the sharp climatological distinction between wet (winter: June through August) and dry (spring/summer: September through March) seasons, with most of annual precipitation falling during the former; and (3) the low prevalence of cloudy conditions during spring and summer months over the mountains, which afford a high availability of remotely sensed snow cover information. Conversely, the SWE reconstruction presented here is certainly subject to a series of uncertainty sources, such as the sparseness of the hydrometeorological observational network, which limits both the availability of forcing and validation data.

However, this is the first estimation of peak SWE and snow depletion distribution at this scale and spatial resolution for the extratropical Andes, and the information shown here can be useful for several applications such as understanding year-to-year differential accumulation patterns that may impact the performance of seasonal streamflow forecast models that rely on point-scale data only. Also, the SWE reconstruction can be used to validate modeling output from global or regional climate models and re-analysis, which are being increasingly employed to estimate hydrological states and fluxes in ungauged regions. By analyzing the spatial correlation of snow accumulation and hydrometeorological variables, distributed SWE estimates can inform the design of improved climate observation networks. Likewise, from analyzing the obtained SWE estimates in light of the necessary modeling assumptions and data availability we are able to highlight future research directions aimed at quantifying and reducing these uncertainties.

The objectives of this research include: to assess the dominant patterns of spatio-temporal variability in snow water equivalent accumulation at scales relevant for hydrological applications in the entire domain of the snow-dominated extratropical Andes cordillera, discussing the implications for water resource availability in the region; and to evaluate the strengths and weaknesses of a pseudo physically based energy balance model of snow melt driven by distributed forcings derived from remotely- and site-based sensors in a sparsely monitored mountain range.

2 Study area

Figure 1 shows the study area, which includes headwater basins in the Andes mountains of central Chile and Argentina, between 27 and 38° S. These basins supply fresh water to low valleys located on both sides of the Cordillera, a topographic barrier more than 5 km high which strongly controls the spatial variability in atmospheric processes (Garreaud, 2009). In Chile, runoff from the Andes Mountains benefits 75 % of the population as well as most of the country's agricultural output, hydropower and industrial activities. In the case of Argentina, 7 % of the population is located in the provinces of La Rioja, San Juan, Mendoza and northern Neuquén, with primary water uses in agriculture and hydropower. The selected watersheds have unimpeded streamflow observations and snow-dominated hydrologic regimes (Fig. 1). Note that the number of headwater basins contained within a continuous spatial domain differs markedly on both sides of the Cordillera due to the transversal valley morphology and arrangement of the gaging stations in the study area, with Argentinean gaging stations being located farther away from the continental divide.

The topography of the central Andes stands out for its high altitude (6000 m a.s.l. ~ 25 to 3000 m a.s.l. ~ 40° S; Montgomery et al., 2001) compared to the average width of 200 km (Garreaud, 2009). The northern area (25 to 30° S) is characterized by the Atacama Desert and transversal valleys on the western slope and Argentinean plains and rolling hills on the eastern slope. Further south (30 to 40° S) the cordillera gradually decreases in elevation, showing a marked asymmetry in the transversal direction expressed within steeper slopes in the western side. At a smaller scale, the topography is dominated by multiple subcatchments arranged in a fan pattern, with rivers running in the east/west direction.

North of the 35° S, an arid–semiarid climate prevails on the western slope, while rainier and moister conditions are characteristic on the eastern slope. South of this latitude, the longitudinal precipitation gradient is reversed (Garreaud, 2009). The hydroclimate is mostly controlled by the orographic effect on precipitation (Falvey and Garreaud, 2007) and inter-annual effects exercised by the Pacific Ocean through the El Niño–Southern Oscillation and Pacific Decadal Oscillation (Masiokas et al., 2006; Newman et al., 2003; Rubio-Álvarez and McPhee, 2010). Precipitation is concentrated in cold winter months in the western slope (Aceituno, 1988) and sporadic spring and summer storms on mountain front plains in the eastern slope are typical of this area. The vegetation cover is markedly different on each side, presenting a steppe type condition in the west slope up to 33° S, transitioning to the south into tall bushes and sparse mountain forest. In the eastern slope instead, the steppe vegetation prevails until 37° S with an intermittent presence of mountain forest in the Patagonian plains (Eva et al., 2004).

Figure 2 summarizes the dominant climatology and associated hydrological regime of rivers in the study region. The hydrological regime is markedly snow-dominated in the northern part of the domain (C1 and C4), with more liquid precipitation contributions to the south (C3 and C8). The most notable differences between the east and west sides of the Andes are the effect of the Altiplanic winter on summer-season precipitation in the northern-east zone and the orographic precipitation gradient in the south-western area. Maximum SWE accumulation is reached between the months of August and September on the western side, while on the eastern side records show that this quantity is reached somewhat later, between late September and early October. Scattered snow showers in mid spring (September through November) affect the study area, but they do not affect significantly the decreasing trend of snow-covered area during the melt season (see timing peak SWE and fSCA analysis in the Supplement). This feature is essential for choosing the SWE reconstruction methodology used in this work, which is only able to represent a decreasing (melting) snowpack. Runoff is partially dictated by glacier contributions which occur in summer. According to the Randolph Glacier Inventory (http://www.glims.org/RGI/) the central Andes cordillera has a glacier area of 2245 km^2 between 27 and 38° S, which is equivalent to 1.5 % of the modeling domain surface area (~ 152 100 km^2).

Title Page
Abstract | Introduction
Conclusions | References
Tables | Figures
◀| |▶
◀ ▶
Back | Close
Full Screen / Esc
Printer-friendly Version
Interactive Discussion

3 Methods

3.1 SWE reconstruction model

A retrospective SWE reconstruction model based on the convolution of the fSCA depletion curve and time-variant energy inputs for each domain pixel was implemented. This method has been extensively applied and tested in various mountain ranges, being adequate under certain conditions. For each year, the model was run at a daily time step between 15 August (end of winter) and 15 January (mid-summer). This time window ensures capturing the most likely time at which peak SWE occurs – which itself is variable from year to year – and the almost complete depletion of the seasonal snowpack. Isolated pixels with non-negative fSCA values may remain after January 15 at glacier and perennial snowpack sites. However, the area fraction that these pixels represent is very low, and can be neglected in the context of this work.

The energy balance model adopted here derives from the formulation proposed by Brubaker et al. (1996), which considers explicit net shortwave and long wave energy terms and a conceptual, pseudo-physically based formulation for turbulent fluxes that depends only on the degree-day air temperature:

$$M_p = \max\{(Q_{\mathrm{nsw}} + Q_{\mathrm{nlw}})f_B + T_{\mathrm{d}}a_{\mathrm{r}}, 0\} \tag{1}$$

Were Q_{nsw} is the net shortwave energy flux; Q_{nlw} is the net longwave energy flux; T_{d} is the degree–day temperature, a_{r} [mm °C^{-1} day^{-1}] is the restricted degree-day factor, and f_B is the energy-to-mass conversion factor with a value of 0.26 [mm W^{-1} m^2 day^{-1}]. Actual melt is obtained by multiplying potential melt by fractional snow cover area:

$$M = M_p\, \mathrm{fSCA}^{\mathrm{fc}} \tag{2}$$

where $\mathrm{fSCA}^{\mathrm{fc}}$ is the fSCA MOD10A1 estimate adjusted to forest cover correction by a vegetation fractional f_{veg} (0 to 1) from the MOD44B product:

$$\mathrm{fSCA}^{\mathrm{fc}} = \frac{\mathrm{fSCA}^{\mathrm{obs}}}{(1 - f_{\mathrm{veg}})} \tag{3}$$

Pixel SWE is computed for each year by accumulating the melt fluxes back in time during the melt season, starting from the day in which fSCA reaches a minimum value (SWE_n), and up to a date such that winter fSCA has plateaued, 15 August (SWE_0) for this region.

$$\mathrm{SWE}_t = \mathrm{SWE}_0 - \sum_{1}^{t} M = M_{t+1} + \mathrm{SWE}_{t+1} \tag{4}$$

$$\mathrm{SWE}_0 = \sum_{t=1}^{n} M_t; \mathrm{SWE}_n = 0 \tag{5}$$

3.2 Fractional Snow Covered Area and land use data

Spatio-temporal evolution of snow covered area was estimated using the Fractional Snow Cover Area (fSCA) product from the Moderate Resolution Imaging Spectroradiometer (MODIS) on-board the Terra satellite (MOD10A1 C5 Level 3). The MOD10A1 product provides, daily fSCA estimates at 500 m resolution. Percentages of snow extent (i.e. 0 to 100 %) are derived from an empirical linearization of the Normalized Difference Snow Index (NDSI), considering the total MODIS reflectance in the visible range (0.545–0.565 µm; band 4) and shortwave infrared (1.628–1.652 µm; band 6) (Hall et al., 2002; Hall and Riggs, 2007).

Binary and fractional MODIS fSCA estimates are limited by the use of an empirical NDSI-based method. These errors are notoriously sensitive to surface features such as fractional vegetation and surface temperature (Rittger et al., 2013). Arsenault et al. (2014) review MODIS fSCA accuracy estimates from several studies under different climatic conditions, reporting a range between 1.5 and 33 % in terms of absolute error with respect to ground observations and operational snow cover datasets. Errors stem mainly from cloud masking and detection of very thin snow (< 10 mm depth), forest cover and terrain complexity. In general, commission and omission errors are higher in early and late snowmelt season (Hall and Riggs, 2007) and decrease with increasing elevation (Arsenault et al., 2014). Molotch and Margulis (2008) compared MODIS and Landsat ETM+ performance in the context of SWE reconstruction, showing that significant differences in SWE estimates were a result of SCA estimation accuracy and less so of model spatial resolution. The latter conclusion supports the feasibility of using the snow covered area products at a 500 m spatial resolution for regional scale studies. Considering this background, we employ the MODIS fSCA product due to (1) an appropriate spatial resolution for modeling large-scale SWE with limited computational resources; and (2) the uniqueness of the NDSI algorithm and the availability of tested methodology for cloud mask post-processing at daily resolution. In order to minimize the effect of cloud cover on the temporal continuity and extent of the fSCA estimates, the MOD10A1 fSCA product was post-processed by a modified algorithm for non-binary products, based on the algorithm proposed by Gafurov and Bárdossy (2009). Their method is adapted here to the fractional snow cover product, applying a three-step correction consisting on: (1) same-pixel linear temporal interpolation over 1, 2 or 3 days prior and posterior to the cloudy pixel, (2) spatial interpolation over the eight-pixel kernel surrounding the cloudy pixel, retaining information from lower-elevation pixels only; and (3) assigning the 2001–2014 fSCA average when steps (1) and (2) where not feasible. This step minimized the effect of cloud cover on data availability over the spatial domain, yielding a 21 % of cloudy pixels in September to 8 % in December.

The Normalized Difference Vegetation Index (NDVI) (Huete et al., 2002) derived from the product MOD13Q1 v5 MODIS Level 3 (16 days – 250 m) is used to classify forest presence for each model pixel. For pixels classified as forested, both fSCA and energy fluxes where corrected: fractional SCA was modified on the basis of percentage forest cover (Molotch, 2009; Rittger et al., 2013), using the average of the forest percentage product MOD44B V51 (Hansen et al., 2003). Forest attenuation (below canopy) on energy fluxes at the snow surface was estimated following the method from Ahl et al. (2006) assuming invariant NDVI over each melt season. The selected NDVI pattern is obtained by averaging the four NDVI scenes available between December–January time window through 14 study years. This time window displays the average state of evergreen forest with the maximum amount of data.

3.3 Model Forcings

Global irradiance under cloudy sky conditions is estimated considering a daily spatial pattern of clear sky irradiance derived by the *r.sun* GRASS GIS module (Hofierka et al., 2002; Neteler et al., 2012) and the clear sky index derived from the insolation incident on a horizontal surface from the "Climatology Resource for Agroclimatology" project in the NASA Prediction Worldwide Energy Resource "POWER" (http://power.larc.nasa.gov/) $1^\circ \times 1^\circ$ gridded product.

A snow-age decay function based on snowfall detection is implemented to estimate daily snow surface albedo (Molotch and Bales, 2006) constrained between values of 0.85 and 0.40 (Army Corps of Engineers – USACE, 1960). Snowfall events were diagnosed using a unique minimum threshold for fSCA increments of 2.5 % for each hydrologic unit area.

Spatially distributed air temperature is generated by combining daily air temperature recorded at index meteorological stations (base stations) and a weekly spatial pattern of skin temperature derived from the Land Surface Temperature (LST) MODIS 1 km × 1 km gridded product (Wan et al., 2004, 2002). The product MOD11A1 V5 Level 3 estimates surface temperature from thermal infrared brightness temperatures (TIR) under clear sky using daytime and nighttime scenes and has been shown to represent adequately measurements at meteorological stations ($R^2 \geq 0.7$), displaying moderate overestimation in spring and underestimation in fall (Neteler, 2010). Other studies have reported similar degree of adjustment, with RSME values around 4.5 K in cold mountain environments (Williamson et al., 2014). Significantly, it is possible to estimate air temperature from the LST product given the high correlation between these two variables (Benali et al., 2012; Colombi et al., 2007; Williamson et al., 2014). Cloud removal post-processing was applied to LST images using the following algorithm: (1) pixel linear temporal interpolation over 1 and 2 weeks prior and posterior to the cloudy pixel; and (2) estimation of remaining null values by an LST-elevation linear regression (Rhee and Im, 2014).

3.4 Spatial extrapolation of model forcings

Spatially distributed forcings are required at each grid element in order to run the SWE reconstruction model. In order to ensure the tractability of the extrapolation process, we divided the model domain into sub-regions or clusters, composed by one or more river basins. The river basins were grouped using a clusterization algorithm based on melt season river flow volume as described in Rubio-Álvarez and McPhee (2010). Then, index variables (air temperature and clear sky index) from corresponding clusters (Fig. 1) are combined with LST and global irradiance to generate spatially explicit forcings coupled with snow surface albedo and MODIS fSCA at 500 m resolution. A further benefit of the clusterization process is that it allows us to analyze distinct regional features of the SWE reconstruction parameters, input variables and output estimates.

Shortwave energy fluxes are estimated as a function of incoming solar radiation based on the equation:

$$Q_{\mathrm{nsw}} = (1 - \alpha_{\mathrm{s}})(G_{\downarrow})\tau_{\mathrm{a}} \tag{6}$$

where α_{s} is snow surface broadband albedo; $G_{\downarrow}$ is incoming solar radiation (irradiance); τ_{a} is the shortwave transmissivity as a function of Leaf Area Index (LAI) for mixed forest cover (Pontailler et al., 2003; Sicart et al., 2004), which in turn is estimated as:

$$\tau_{\mathrm{a}} = e^{(-\kappa \mathrm{LAI})}; \mathrm{LAI} = -1.323 \ln\left(\frac{0.88 - \mathrm{NDVI}}{0.72}\right) \tag{7}$$

with $\kappa = 0.52$ for mixed forest species (Dewalle and Rango, 2008). Equation (8) is valid for NDVI values between 0.16 and 0.87. Spatially distributed solar radiation patterns were estimated through the computation of clear sky irradiance, $G_{\mathrm{c}\downarrow}$, with the *r.sun* routine multiplied by a daily cloud fraction coefficient (K_{c}), which was assumed homogeneous for each cluster. The K_{c} coefficient is estimated as the rate between clear sky solar radiation (1° × 1° gridded product – $\overline{G_{r\downarrow}}$) and *r.sun* clear sky solar radiation product ($\overline{G_{\mathrm{c}\downarrow}}$), considering both the spatial average over each cluster:

$$G_{\downarrow} = K_{\mathrm{c}} G_{\mathrm{c}\downarrow}; K_{\mathrm{c}} = \left(\overline{G_{\mathrm{r}\downarrow}}/\overline{G_{\mathrm{c}\downarrow}}\right) \tag{8}$$

Long wave energy fluxes are parameterized as a function of air temperature (T_{a}), snow surface temperature (T_{s}), snow emissivity ($\varepsilon_{\mathrm{s}} = 0.97$), sky-view factor ($f_{\mathrm{sv}}$) assumed equal to shortwave transmissivity (Pomeroy et al., 2009; Sicart et al., 2004), the Stefan-Boltzmann constant (σ) and incoming long wave radiation $L_{\downarrow}$. The equations relating all these terms are:

$$Q_{\mathrm{nlw}} = L_{\downarrow} f_{\mathrm{sv}} \varepsilon_{\mathrm{s}} + \sigma T_{\mathrm{a}}^{4} (1 - f_{\mathrm{sv}}) \varepsilon_{\mathrm{sf}} - \sigma T_{\mathrm{s}}^{4} \varepsilon_{\mathrm{s}} \tag{9}$$

$$L_{\downarrow} = 0.575\, e_{\mathrm{a}}^{1/7} \sigma T_{\mathrm{a}}^{4} (1 + a_{\mathrm{c}} C^{2}) \tag{10}$$

Daily mean air temperature is extrapolated by means of relating the spatial variability observed between meteorological stations and between grid elements in the MODIS LST product. Defining ΔT_{a} as the difference in air temperature between two stations located at high altitude and valley sites, while $T_{\mathrm{a\ base}}$ is the daily index station air temperature, air temperature at any model pixel is given by the addition of both terms. To determine ΔT_{a} we use a linear regression performed between MODIS LST delta (ΔLST) and ΔT_{a} considering pairs of stations located at high altitude (has) and valley (base) sites, taking into account the melt season average values over the 2001–2014 period. After that, we proposed an air temperature extrapolation by:

$$T_{\mathrm{a}} = T_{\mathrm{a\ base}} + \Delta T_{\mathrm{a}} = T_{\mathrm{a\ base}} + \mu(\mathrm{LST} - \mathrm{LST}_{\mathrm{base}}) + \nu \tag{11}$$

were LST – $\mathrm{LST_{base}}$ denotes the difference between skin temperatures from any pixel and the index station, unique to a particular cluster. In Eq. (11), ($R^2 = 0.93$) and μ (0.65) and ν (–0.5) are the slope and offset, respectively of the regression relationship (Fig. S3 in the Supplement). This spatial extrapolation method was preferred over more traditional methods – for example based on vertical lapse-rates (Minder et al., 2010; Molotch and Margulis, 2008) – after initial tests showed that the combined effect of the relatively low elevation of index stations and the large vertical range of the study domain resulted in unreasonably low air temperatures at pixels with the highest elevations. Likewise, the scarcity of high-elevation meteorological stations and the large spatial extent of the model domain precluded us from adopting more sophisticated temperature vertical gradients with confidence (e.g. Ragettli et al., 2014).

Air vapor pressure (required for long wave parametrization) is estimated from air temperature and relative humidity, which in turn was assumed constant throughout the melt period and equal to 40 % based on observations at selected high-elevation meteorological stations. The multiplying factor $(1 + a_c C^2)$ represents an increase in energy input relative to clear sky conditions due to cloud cover, where a_c equals 0.17 and $C = 1 - K_c$ is an estimate of the cloud cover fraction proposed for this paper (DeWalle and Rango, 2008). Snow surface temperature and degree-day temperature are estimated (Brubaker et al., 1996) as:

$$T_d = \max(T_a, 0)\,;\; T_s = \min(T_a - \Delta_T, 0) \quad (12)$$

where Δ_T is the difference between air and snow surface temperature. This value is highly variable in time and space, and few direct, systematic observations exist in our study area. Therefore, we adopt an average value $\Delta_T = 2.5$ [°C], following the suggestion in Brubaker et al. (1996). Slightly higher values ranging from 3 to 6 °C are shown for continental and alpine snow types (Raleigh et al., 2013) evidencing an additional source of uncertainty over net long wave computations. More sophisticated parametrizations for T_s, for example based on heat flow through the snowpack, have been proposed (e.g. Rankinen et al., 2004; Tarboton and Luce, 1996) but those require explicit knowledge about the snowpack temperature profile and/or more complex model formulations to estimate the internal snowpack heat and mass budgets simultaneously. Available data in our study area is still insufficient to understand the spatio-temporal evolution of this variable, thus we adopt a simpler, more parsimonious model for this application.

The a_r coefficient in the restricted degree-day energy balance equation was computed using a combination of station and reanalysis data, and assumed spatially homogeneous within each of the clusters that subdivide the model domain. Brubaker et al. (1996) propose a scheme in which this parameter can be explicitly computed from air and snow surface temperature, air relative humidity, and atmospheric pressure and wind speed. The resulting equation is:

$$a_\mathrm{r} = f_B \rho C_\mathrm{h} k^2 \ln(z/z_0)^{-2} u \left[c_p + \mathrm{RH_a} \frac{L}{2} \frac{0.622}{p} \left(\frac{\mathrm{d}e^*}{\mathrm{d}T} \right)_0 - \frac{(1-\mathrm{RH_a})}{T_\mathrm{a}} \frac{L}{2} \frac{0.622}{p} e_0^* \right] \qquad (13)$$

Wind speed was obtained from the NASA POWER reanalysis described previously. A correction for atmospheric stability is applied on the bulk transfer coefficient C_h according to the formulation presented by Kustas et al. (1994), assuming a surface roughness of 0.0005 m:

$$C_\mathrm{h} = \left\{ \begin{array}{l} (1-58R_i)^{0.25} \text{ for } R_i < 0 \\ (1+7R_i)^{-0.1} \text{ for } R_i > 0 \end{array} \right\} ; R_i = \frac{gz(T_\mathrm{a} - T_\mathrm{s})}{u^2 T_\mathrm{a}} \qquad (14)$$

Where R_i is the Richardson number, g is the gravity acceleration (9.8 [$\mathrm{m\,s^{-2}}$]), z is the standard air temperature measurement height (2 m) and u is wind speed. The calculation of R_i and a_r is based on the standard assumptions of T_s at the freezing point and a water vapor saturated snow surface over all high-elevation meteorological stations with available air temperature and relative humidity records (Molotch and Margulis, 2008). Further in the text, we discuss some implications of these assumptions and of the input data used on the ability of the model of simulating relevant components of the snowpack energy exchange.

Table 1 shows the main cluster characteristics and regionalized model parameters. It can be seen that for those clusters located in the southern and middle reaches of the model domain, the a_r parameter reaches general values in the vicinity of 0.11–0.23 [cm °C^{-1} day^{-1}], which is similar to values reported in previous studies performed in other mountain ranges in the Northern Hemisphere (0.20–0.25 in Martinec, 1989; 0.17 in Kustas et al., 1994; 0.20 in Brubaker at al., 1996; 0.15 in Molotch and Margulis, 2008). However, values associated to the northernmost clusters of our study area are quite low, reaching under 0.02 for the C1 cluster in northern Chile.

Clear sky index values range between 0.78 and 0.89. Salazar and Raichijk (2014) estimate K_c values on the order of 0.90 for a single location at 1200 m a.s.l. in northern Argentina, based on station data. Our estimates are slightly lower, more so on clusters C1 and C4, but the general temporal variability in our estimations is similar to that reported in their work. A 5 to 6 °C difference can be observed in mean air temperature at index stations between the northern and southern edge of the domain. Temperatures for the C4 cluster are subject to greater uncertainty, because no high-elevation climate station data was available for this study. Forest cover values are lower than 6 % throughout the model domain, with the exception of cluster C3, with a value of 13.8 %. The difference in forest cover between clusters C3 and C8 can be attributed to the precipitation shadow effect induced by the Andes ridge, because other relevant attributes (average latitude, elevation) are very similar among these areas. Forest corrections applied to MODIS fSCA resulted in a 17 % increase at the southern sub-domain (C3).

3.5 Validation data: SWE, snow depth and river flow observations

Operational daily snow-pillow data from stations maintained by government agencies in Chile and Argentina were available for this study (Table 2). Only stations with ten or more years of record were included and manual snow course data were neglected because of their discontinuous nature. Approximately 10 % of observed maximum SWE accumulation values were discarded due to obvious measurement errors and data gaps. An analysis of the seasonal variability of snow-pillow records on the western and

Title Page
Abstract Introduction
Conclusions References
Tables Figures
◀◀ ▶▶
◀ ▶
Back Close
Full Screen / Esc
Printer-friendly Version
Interactive Discussion

eastern slopes of the Andes suggests that peak-SWE date is somewhat delayed on the latter, by approximately one month. Therefore, peak-SWE estimates for Chilean and Argentinean stations are evaluated on 1 September and 1 October, respectively. Manual snow depth observations were taken in the vicinity of selected snow-pillow locations in order to evaluate the representativeness of these measurements at the MODIS grid scale during the peak-SWE time window. These depth observations were obtained in regular grid patterns within an area the approximate size of a MODIS pixel (500 m), centered about the snow-pillow location. Observations were spaced at 50 m increments approximately, and multiplied by density observations obtained at snow-pits dug adjacent to the pillow sites. Snow density was estimated by a weighted average of snow densities measured in snow pits with a 1000-cc snow cutter. Samples where obtained either at regular 10 cm depth intervals along the snow pit face, or at the approximate mid depth of identifiable snow strata for very shallow snow pack conditions. Weights were computed as the fraction of total depth represented by each snow sample.

Distributed snow depth observations were available from snow surveys carried out during late winter between 2010 and 2014 at seven study catchments in the western side of the Andes, between latitudes 30 and 37° S (Fig. 1, Table 2). Snow depths were recorded with 3 m graduated avalanche probes inserted vertically into the snow pack. Depending on the terrain conditions, between three and five individual point snow depth measurements were obtained at each location, from which a mean snow depth and standard error were calculated (three point observations were forming a line with a distance of one meter and five point observations were forming a cross with an angle of 90 ° and a point distance of one meter). Pixel-scale SWE estimates were obtained by averaging all depth observations within the limits of MODIS pixels and multiplying them by density observations from snow pits excavated at the time of each snow survey (two or three snow pits per field campaign). After this, individual depth observations were converted into SWE for model validation. Modeled SWE values were averaged at all MODIS pixels where manual depth observations are available, and their summary statistics are compared to those of SWE estimated from manual depth observations at the same pixels, multiplied by average density from snow pits. All spatial statistics are direct calculations, with no further geo-processing of manual observations.

Spring and summer season (September to March) total river flow volume (SSRV) for the 2001–2014 period were obtained from unimpaired streamflow records at river gauges located in the mountain front along the model domain. Data were verified through standard hydrological procedures in order to discard anomalous values and to ensure homogeneity throughout the period of study. Regional consistency was verified through regression analysis, only including streamflow records with $R^2 > 0.50$ among neighboring catchments. Missing values (3.7 % of the entire period) were filled through linear regression.

4 Results

4.1 Model validation

Figure 3 compares reconstructed peak SWE (gray circles) to observed values at three snow-pillow locations (black diamonds) where additional validation sampling at the MODIS pixel scale was conducted (box plots). At the Cerro Vega Negra site (CVN), located in cluster C1, the model overestimates peak SWE (1 September) with respect to the snow-pillow value by 97 % in 2013 and 198 % in 2014. At the Portillo site (POR, cluster C2), reconstructed SWE underestimates recorded values by 51 % in 2013 and 72 % 2014. At the Laguna Negra site (LAG, also C2), reconstructed peak SWE slightly overestimates recorded values (8 %) (Table 4). However, reconstructed SWE compares favorably to distributed manual SWE observations obtained in the vicinity of the snow pillows at the POR and LAG sites.

Figure 4 depicts the comparison between reconstructed SWE and snow surveys carried out at pilot basins throughout the model domain. From left to right, it can be seen that the model slightly overestimates SWE with respect to observations at CVN

(18 % overestimation), except in 2012. Further south, there is a very good agreement at ODA–MAR (4 % underestimation), and then the model underestimates SWE at MOR–LVD (39 % underestimation) and OB–RBL (36 % underestimation). Of all study basins, CHI is the only one with significant forest cover. Here the model significantly underestimates SWE with respect to manual samples at forested sites (67 %), displayed in the 2013b and 2014b plots. For the 2013a and 2014a boxes – which correspond to clearing sites – there is still underestimation, but of lesser magnitude (20 %). Summarizing, we detect model overestimation respect to snow survey medians in four cases and underestimation in fifteen cases. In 11 out of 19 cases, reconstructed SWE lies within the snow survey data uncertainty bounds (standard deviation).

Extending the comparison to all snow-pillow sites included in this study, Fig. 5 suggests that the model tends to overestimate observed peak SWE at the two northernmost sites on the Chilean side (QUE and CVN). The equivalent cluster on the Argentinean side (C4) lacks SWE observations. These comparisons must be interpreted taking into account that point-values with a support of a few squared meters are being contrasted to 500 m × 500 m pixel estimates, and a host of local factors including wind transport, preferential deposition due to perimeter fences, and instrumental errors may affect the representativeness of snow-pillow data with respect to the model grid cell. Overall, we find a better agreement at the eastern slope sites ($R^2 = 0.74$) than at their west counterparts ($R^2 = 0.43$), with a combined R2 value of 0.61. Individually, the worst and best linear agreements are obtained at POR ($R^2 = 0.32$) and LOA ($R^2 = 0.88$), respectively. Average standard error $\mathrm{SE}_{\overline{x}}$ is 284 mm ($\mathrm{SE}_{\overline{x}} = 242$ mm at the west slope; $\mathrm{SE}_{\overline{x}} = 302$ mm at the east slope), with a range between 72 mm (TOS) and 378 mm (ATU) (Table 4). Relative errors display some variability, with overestimation higher than 30 % at the two northernmost (QUE and CVN) and at the southernmost (PEH) snow pillows. For all other snow pillows, the model underestimates with respect to the sensor observation; the range of relative errors for those sites with underestimation goes from −52 to −5 %.

A final exercise is carried out considering seasonal river flow volume recorded at selected stream gauges. Under the assumption of unimpaired flows (no human extractions), peak SWE and seasonal flow volume should show some degree of correlation, even though no assumptions can be made here about other relevant hydrologic processes, such as flow contributions from glaciated areas, subsurface storage carryover at the basin scale and influence of spring and summer precipitation. Differences can be expected due to losses to evapotranspiration and sublimation affecting the snowpack and soil water throughout the melt season, so at least conceptually basin-averaged peak SWE should always be higher than melt season river volume. A clear regional pattern emerges when inspecting the results of this comparison in Fig. 6. Correlation between peak SWE and melt season river flow is higher in clusters C1 and C4 with R2 values of 0.84 and 0.86, respectively. The result for Cluster C4 indicates that liquid precipitation during the melt season (which from Fig. 2 may be considered significant), does not result in decreased correlation between peak SWE and river flow. Clusters C2, C5, C6 and C7 display a somewhat lower correlation, with some individual years departing more significantly from the overall linear trend. R2 values range between 0.46 and 0.67 in these cases. Finally, not only are correlation coefficients lower for the southern clusters C3 (R2 = 0.56) and C8 (R2 = 0.48), but also estimated peak SWE is always lower than river flow, which indicates the importance of spring and summer precipitation in determining streamflow variability. In fact, Castro et al. (2014) analyze patterns of daily precipitation in this area and document average spring and summer rainfall amounts of approximately in order to 520 mm (C3) and 85 mm (C8).

4.2 Regional SWE estimates

Figure 7 shows the September 15 SWE average over the 2001–2014 period obtained from the reconstruction model, and the percent annual deviations (anomalies) from that average. Steep elevation gradients can be inferred from the climatology, as well as the latitudinal variation expected from precipitation spatial patterns. For the northern clusters (C1 and C4), the average peak SWE is in the order of 165 mm SWE while the middle section of the domain reaches peak SWE averages of approximately 400 mm. The southern clusters (C3, C7, C8) do show similar accumulation averages, despite the sharp decrease in the Andes elevation south of latitude 34° S. The anomaly maps convey the important degree of inter-annual variability, as well as distinct spatial patterns associated with it. Between 2001 and 2014, years 2002 and 2005 stand out for displaying large positive anomalies throughout the entire mountainous region of the model domain, with values 2000 mm and more above the simulation period average. Other years prior to 2010 show differential accumulation patterns, where either the northern or southern parts of the domain are more strongly affected by positive or negative anomalies. Overall, the northern clusters (C1 and C4) show above-average accumulation in only three (2002, 2005 and 2007) of the 14 simulated years, whereas the other clusters show above-average accumulation on six years (2001, 02, 05, 06, 08 and 09). In particular, years 2007 and 2009 show a bimodal spatial structure, with excess accumulation (deficit) in the northern (southern) clusters during the former, and the inverse pattern in the latter year.

A longitudinal pattern in the distribution of negative anomalies can be discerned from Fig. 7, whereby during deficit years one or other side of the water divide concentrates the higher deficits with respect to the period mean. On the other hand, during positive anomaly years, both sides of the Andes seem to share the excess accumulation. Further research on the mechanisms of moisture transport during below-average precipitation years may shed light on this result. Since 2009 it is possible to observe the effects of a drought that has developed over the entire model domain.

Figure 8 provides a different perspective on the region's peak SWE climatology by presenting our results aggregated into elevation bands for each hydrologic unit. Elevation bands are defined at 1000 m increments starting from 1000 m a.s.l. Crosses indicate average peak SWE for each band (mm), and circle areas are proportional to the surface area covered by each elevation band. From north to south, hydrologic unit C4 shows slightly higher SWE than C1 between 3000 and 5000 m a.s.l., but much larger surface areas (~ 32 000 vs. ~ 17 000 km^2), indicating a larger water resource potential. Interestingly, the band between 5000 and 6000 m a.s.l. presents more than 500 mm and ~ 1800 km^2 of surface area in C4, whereas for C1 the contribution of this band, in terms of SWE and surface area, is much smaller. C2 stands out as having the largest area-weighted SWE in the model domain, overall and for each elevation band. Compared to its counterpart on the eastern side of the Andes range (C5), C2 shows higher accumulations at all elevations. Particularly relevant is the large area covered between 2000 and 4000 m a.s.l. (~ 13 000 km^2), combined with peak accumulation in the order of 600 mm. Although the 4000–5000 m a.s.l. elevation band contributes approximately half the surface area in C2, its average peak SWE is roughly twice that of the 3000–4000 band (~ 6000 km^2). This makes this subregion interesting for future research, because most snow observations in the area are obtained below 4000 m a.s.l. (the same is true for unit C5). Further to the south, the barrier effect of the Andes is also suggested by the displacement of the swe-elevation distribution in C6, C7 compared to C3. On the eastern side of the model domain, it is interesting to see a steepening of the average peak SWE elevation profile between C6 and C8, suggesting that C8 is less affected by Andes blockage than its northern counterparts.

Estimated net energy inputs (Fig. 9) show a spatial pattern, with values that decrease from the northern (C1 and C4) into the mid-range clusters (C2, C5 and C6), to increase again with latitude into the southern reaches of the domain (C3, C7 and C8). This is a result of a combination of an increasing trend in net shortwave radiation in the south–north direction and a reverse spatial trend in net long wave radiation exchange, which increases (approaches less-negative values) in the north–south direction. Modeled turbulent energy fluxes ($T_\text{d} \cdot a_\text{r}/f_B$) are negligible in the northern clusters, but their contribution to the net energy exchange increases with latitude as a result of the spatial variation in the a_r parameter.

Figure 10 shows the temporal (seasonal) variation in average fSCA and SWE for each cluster, and Table 5 shows peak SWE at the watershed scale, averaged both over the entire basin and over the snow covered area. Maximum fSCA increases in the north–south direction, consistently with the climatological increase in winter precipitation and decrease in temperature (which override the lowering of the Andes elevation). A dramatic increase in snow coverage is observed between the northern (C1 and C4) and their adjacent-to-the-south (C2 and C5) clusters, with average peak fSCA increasing from 20 to 50 %. The highest average snow coverage is observed for cluster C8, with more than 60 %. Snow water equivalent displays a similar regional variability, but lower seasonal variability than snow cover for all clusters except for C2 (central Chile), where fSCA and SWE variability throughout the melt season are identical. Mean peak SWE in northern Chile is the lowest among the eight clusters, with approximately 100 mm SWE over the 2001–2014 period. The largest estimate is for cluster C2, central Chile, where mean peak SWE exceeds 500 mm. The rain shadow effect of the Andes range is apparent in the comparison estimates at C2 and C5–C6–C7. Not only fSCA is lower (affected by the larger basin sizes on the Argentinean side), but also peak SWE is approximately 25 % lower, with less than 400 mm SWE for the eastern clusters. Cluster C4 is not affected by this phenomenon, showing higher snow coverage and water equivalent accumulation than its counterpart, C1. Cluster C8 represents an interesting exception in that its average fSCA is the largest within the model domain, but peak SWE is not significantly higher than the estimates in the other clusters on the Argentinean side of the Andes.

5 Discussion

5.1 Sensitivity analysis

The Andes cordillera, on one hand, displays ideal conditions for SWE reconstruction, including low cloud cover, infrequent snowfall during spring and summer, and very low forest cover. On the other hand, the scarcity of basic climate data poses challenges that would affect any modeling exercise. A local sensitivity analysis is implemented in order to gain insights regarding the influence of some of the assumptions required for SWE modeling (Fig. 11). The influence of the clear sky factor (K_c), snow surface albedo

($\propto_s$), the slope of the Δ_{LST} vs. Δ_{Ta} relationship (μ), the a_r parameter, and the difference between air and snow surface temperature are explored. Results are shown for the model pixels corresponding to two of the snow pillow sites, each located at the northern and southern sub-regions of the model domain respectively. The clear sky factor, snow albedo and Δ_{LST} vs. Δ_{Ta} slope are the most sensitive parameters at the northern (CVN) site. Increasing the slope in the Δ_{LST} vs. Δ_{Ta} relationship results in decreasing air temperature at pixels with higher elevations than the index station, thus lowering long wave exchange and resulting in lower SWE estimates. The impact of decreasing slope values results in a marked increase in SWE due to increased pixel air temperature, but snow surface temperature is limited from above at 0 °C. The influence of snow albedo is analyzed by perturbing the entire albedo time series for each season from the values predicated by the USACE model. Increasing albedo values restricts the energy available for melt therefore decreasing peak SWE estimates. Again, a nonlinear effect is observed, constrained from below by the 0.4 minimum albedo value, which was not altered during the sensitivity experiment. The sensitivity of the clear sky factor, on the other hand, is monotonic, with increasing values generating more available solar energy, resulting in higher SWE estimates. At the southern site (ALT), the shape of the sensitivity functions is the same as at CVN, but the magnitude of SWE variations as a function of parameter perturbations is smaller. This is likely related to the fact that turbulent fluxes constitute a larger fraction of the simulated overall energy balance at the southern sites – because of the larger values of the a_r parameter –, therefore perturbations over the other terms account for a smaller fraction of the energy exchange. At the southern site, we see an increase in the sensitivity of the a_r parameter, most likely related to its larger initial magnitude compared with that at CVN, which make turbulent fluxes a more relevant component of the snowpack energy budget.

5.2 Conceptual energy balance model representation

Figure 12 describes the spatial distribution of the a_r parameter, and its dependence on air temperature and relative humidity observed at index meteorological stations. The implication for energy balance modeling is that turbulent fluxes would account for a very small portion of the snowpack energy and mass balance in the northern area (C1 and C4), which is characterized by low air temperatures and relative humidity, which yield very low a_r values. The reader must recall that a_r values were computed based on index station data and assumed spatially homogeneous over each cluster. The simplified model formulation used in this research, however, although pseudo-physically based – compared to degree-day or fully calibrated models – allows only for positive net turbulent fluxes, because both the a_r and the degree-day temperature index are positive values. However, previous studies in this region (Corripio and Purves, 2005; Favier et al., 2009) have suggested that latent heat fluxes have a relevant role because of high sublimation rates favored by high wind and low relative humidity conditions predominant in the area.

In order to diagnose differential performance of the model across the hydrologic units defined in this study, we compute the Bowen ratio (β) at the point scale from data available only at the few high elevation meteorological stations in the region (with recorded relative humidity). This ratio confirms that for the stations located within cluster C1, latent heat fluxes have opposite sign and dominate over sensible heat fluxes (Fig. S6 in Supplement) which results in net turbulent cooling of the snowpack. Note that for the clusters C5, C6, C7 and C8, all located on the eastern (Argentinean) slope of the Andes, sensible and latent heat fluxes are positive, compared to negative latent heat fluxes for all the index stations within clusters C2 and C3 on the Chilean side. This result is coherent with that reported by Insel et al. (2010), who applied a Regional Circulation Model (RegCM3) in the area and showed a notorious difference in terms of air relative humidity ($\sim 70\,\%$ east side vs. $\sim 40\,\%$ west side), which would support the notion of more significant condensation on the eastern side of the continental divide. The fact that we extrapolate the a_r parameter value based on these meteorological observations throughout the southern Argentinean hydrologic units may result in a yet not quantified overestimation of seasonal energy inputs and peak SWE for those clusters.

6 Conclusions

Snow water equivalent is the foremost water resource precursor for the extratropical Andes region in South America. This paper presents the first high-resolution distributed assessment of this critical resource, combining instrumental records with remotely sensed snow covered area and a physically-based snow energy balance model. Overall errors in estimated peak SWE when compared with operational station data amount to −2 %, and correlation with observed melt-season river flows in high, with a value of 0.55. The current state development of remotely sensed products allowed us to apply the reconstruction model with almost no calibration, representing realistically the most relevant components of the snowpack energy balance. MODIS Fractional SCA data proved adequate for the goals of this study, affording high temporal resolution and an appropriate spatial resolution given the extent of the study region. Likewise, remotely sensed surface temperature showed good agreement with station data and allowed the estimation of spatially distributed temperature fields.

Overall, the model performance evaluated against SWE observations is comparable to that achieved in other mountain regions of the world. Our overall coefficient of determination R2 of 0.61 is lower than that obtained by Guan et al. (2013) in the Sierra Nevada (0.74) when comparing operational snow pillow observations. The overall relative error is −2 % for observations from snow pillows our study region, but this value is strongly affected by two stations where we observed significant overestimation (QUE and CVN). When including the remaining ten snow pillows only, relative error increases to −16 %. Regional SWE and anomaly estimates illustrate the dramatic spatial and temporal variability of water resources in the extratropical Andes, and provide a striking visual assessment of the progression of the drought that has affected the region since 2009. These results should motivate further research looking into the climatic precursors of this spatially distributed phenomenon.

The results presented here have several potential applications. For the evaluation of seasonal forecasting models that rely on point-scale data, the analysis of past differential accumulation patterns and their synoptic-scale precursors may prove useful in fine tuning models for higher skill in years showing un-common atmospheric circulation patterns. Precipitation and snow components in regional and global climate models and reanalyses can be evaluated using the precipitation-independent SWE estimates presented here. Differential accumulation patterns across elevation bands suggest that the 4000–5000 m a.s.l. region is a significant contributor of water resources for the region, but little or no information exists on snow properties at those elevations. Finally, the evaluation of alternative water resource projects as part of development and climate change adaptation initiatives can be enhanced by assessing the spatially distributed nature of snow in ungauged basins, given the strong correlation we show between peak SWE and seasonal river flow for the majority of analyzed basins.

Accurate representation of spatially distributed model forcings remains an important challenge in remote areas such as the extratropical Andes. However, the low frequency of cloudy conditions, scarce forest cover (3.3 %) and the sharp temporal differences between accumulation and melt season snowfall, allow us to analyze the strengths and weaknesses of the modeling approach, discriminating model and observation errors. Future work must strive to assess sources and quantify the uncertainty in these SWE estimates, resulting from fSCA and energy flux imprecisions, which in this work may compensate with each other. Distributed snow albedo estimates based on robust modeling and remotely sensed data should improve estimations, particularly at a local scale. Workable turbulent flux parameterizations in areas where sublimation is significant should be sought for, moreover because these areas are subject to significant water stress.

The Supplement related to this article is available online at doi:10.5194/hessd-12-8927-2015-supplement.

Acknowledgements. This research was conducted with support from CONICYT, under grants FONDECYT 1121184, SER-03, FONDEF CA13I10277 and CHILE-USA2013. The authors wish to thank everybody involved in field data collection, included brothers Santiago and Gonzalo Montserrat, Mauricio Cartes, Alvaro Ayala, and many others. Gonzalo Cortés provided insightful comments to working drafts of this manuscript.

References

Aceituno, P.: On the functioning of the Southern Oscillation in the South American sector. Part I: Surface climate, Mon. Weather Rev., 116, 505–524, 1988.

Ahl, D. E., Gower, S. T., Burrows, S. N., Shabanov, N. V., Myneni, R. B., and Knyazikhin, Y.: Monitoring spring canopy phenology of a deciduous broadleaf forest using MODIS, Remote Sens. Environ., 104, 88–95, 2006.

Aravena, J.-C. and Luckman, B. H.: Spatio-temporal rainfall patterns in southern South America, Int. J. Climatol., 29, 2106–2120, 2009.

Army Corps of Engineers: Engineering and Design: Runoff From Snowmelt, Washington, 1960.

Arsenault, K. R., Houser, P. R., and De Lannoy, G. J. M.: Evaluation of the MODIS snow cover fraction product, Hydrol. Process., 28, 980–998, doi:10.1002/hyp.9636, 2014.

Ayala, A., McPhee, J., and Vargas, X.: Altitudinal gradients, midwinter melt, and wind effects on snow accumulation in semiarid midlatitude Andes under La Niña conditions, Water Resour. Res., 50, 3589–3594, doi:10.1002/2013WR014960, 2014.

Benali, A., Carvalho, A. C., Nunes, J. P., Carvalhais, N., and Santos, A.: Estimating air surface temperature in Portugal using MODIS LST data, Remote Sens. Environ., 124, 108–121, 2012.

Brubaker, K., Rango, A., and Kustas, W.: Incorporating radiation inputs into the snowmelt runoff model, Hydrol. Process., 10, 1329–1343, doi:10.1002/(SICI)1099-1085(199610)10:10<1329::AID-HYP464>3.0.CO;2-W, 1996.

Castro, L. M., Gironás, J., and Fernández, B.: Spatial estimation of daily precipitation in regions with complex relief and scarce data using terrain orientation, J. Hydrol., 517, 481–492, 2014.

Cline, D. W., Bales, R. C., and Dozier, J.: Estimating the spatial distribution of snow in mountain basins using remote sensing and energy balance modeling, Water Resour. Res., 34, 1275–1285, 1998.

Colombi, A., De Michele, C., Pepe, M., and Rampini, A.: Estimation of daily mean air temperature from MODIS LST in Alpine areas, EARSeL EProceedings, 6, 38–46, 2007.

Corripio, J. G. and Purves, R. S.: Surface energy balance of high altitude glaciers in the central Andes: The effect of snow penitentes, Clim. Hydrol. Mt. Areas, 15–27, 2005.

Cortés, G., Vargas, X., and McPhee, J.: Climatic sensitivity of streamflow timing in the extratropical western Andes Cordillera, J. Hydrol., 405, 93–109, doi:10.1016/j.jhydrol.2011.05.013, 2011.

Cortés, G., Girotto, M., and Margulis, S. A.: Analysis of sub-pixel snow and ice extent over the extratropical Andes using spectral unmixing of historical Landsat imagery, Remote Sens. Environ., 141, 64–78, doi:10.1016/j.rse.2013.10.023, 2014.

DeWalle, D. and Rango, A.: Principles of Snow Hydrology, Cambridge University Press, New York, 2008.

Dietz, A. J., Kuenzer, C., Gessner, U., and Dech, S.: Remote sensing of snow–a review of available methods, Int. J. Remote Sens., 33, 4094–4134, 2012.

Eva, H. D., Belward, A. S., De Miranda, E. E., Di Bella, C. M., Gond, V., Huber, O., Jones, S., Sgrenzaroli, M., and Fritz, S.: A land cover map of South America, Glob. Change Biol., 10, 731–744, 2004.

Falvey, M. and Garreaud, R.: Wintertime precipitation episodes in central Chile: Associated meteorological conditions and orographic influences, J. Hydrometeorol., 8, 171–193, 2007.

Falvey, M. and Garreaud, R. D.: Regional cooling in a warming world: Recent temperature trends in the southeast Pacific and along the west coast of subtropical South America (1979–2006), J. Geophys. Res.-Atmos., 114, D04102, doi:10.1029/2008JD010519, 2009.

Favier, V., Falvey, M., Rabatel, A., Praderio, E., and López, D.: Interpreting discrepancies between discharge and precipitation in high-altitude area of Chile's Norte Chico region (26–32° S), Water Resour. Res., 45, W02424, doi:10.1029/2008WR006802, 2009.

Gafurov, A. and Bárdossy, A.: Cloud removal methodology from MODIS snow cover product, Hydrol. Earth Syst. Sci., 13, 1361–1373, doi:10.5194/hess-13-1361-2009, 2009.

Garreaud, R. D.: The Andes climate and weather, Adv. Geosci., 22, 3–11, doi:10.5194/adgeo-22-3-2009, 2009.

Gascoin, S., Lhermitte, S., Kinnard, C., Bortels, K., and Liston, G. E.: Wind effects on snow cover in Pascua-Lama, dry Andes of Chile, Adv. Water Resour., 55, 25–39, doi:10.1016/j.advwatres.2012.11.013, 2013.

Guan, B., Molotch, N. P., Waliser, D. E., Jepsen, S. M., Painter, T. H., and Dozier, J.: Snow water equivalent in the Sierra Nevada: blending snow sensor observations with snowmelt model simulations, Water Resour. Res., 49, 5029–5046, doi:10.1002/wrcr.20387, 2013.

Hall, D. K. and Riggs, G. A.: Accuracy assessment of the MODIS snow products, Hydrol. Process., 21, 1534–1547, 2007.

Hall, D. K., Riggs, G. A., Salomonson, V. V., DiGirolamo, N. E., and Bayr, K. J.: MODIS snow-cover products, Remote Sens. Environ., 83, 181–194, 2002.

Hansen, M. C., DeFries, R. S., Townshend, J. R. G., Carroll, M., Dimiceli, C., and Sohlberg, R. A.: Global percent tree cover at a spatial resolution of 500 m: first results of the MODIS vegetation continuous fields algorithm, Earth Interact., 7, 1–15, 2003.

Hofierka, J. and Suri, M.: The solar radiation model for Open source GIS: implementation and applications, in: Proceedings of the Open source GIS – GRASS users conference 2002, Trento, Italy, 11–13 September 2002.

Huete, A., Didan, K., Miura, T., Rodriguez, E. P., Gao, X., and Ferreira, L. G.: Overview of the radiometric and biophysical performance of the MODIS vegetation indices, Remote Sens. Environ., 83, 195–213, 2002.

Insel, N., Poulsen, C. J., and Ehlers, T. A.: Influence of the Andes Mountains on South American moisture transport, convection, and precipitation, Clim. Dynam., 35, 1477–1492, 2010.

Jepsen, S. M., Molotch, N. P., Williams, M. W., Rittger, K. E., and Sickman, J. O.: Interannual variability of snowmelt in the Sierra Nevada and Rocky Mountains, United States: examples from two alpine watersheds, Water Resour. Res., 48, W02529, doi:10.1029/2011WR011006, 2012.

Kustas, W. P., Rango, A., and Uijlenhoet, R.: A simple energy budget algorithm for the snowmelt runoff model, Water Resour. Res., 30, 1515–1527, 1994.

Martinec, J.: Hour-to-hour snowmelt rates and lysimeter outflow during an entire ablation period, Snow Cover Glacier Var., IAHS Publ. no. 183, 19–28, 1989.

Masiokas, M. H., Villalba, R., Luckman, B. H., Le Quesne, C., and Aravena, J. C.: Snowpack variations in the central Andes of Argentina and Chile, 1951–2005: large-scale atmospheric influences and implications for water resources in the region, J. Climate, 19, 6334–6352, 2006.

Minder, J. R., Mote, P. W., and Lundquist, J. D.: Surface temperature lapse rates over complex terrain: lessons from the Cascade Mountains, J. Geophys. Res.-Atmos., 115, 1984–2012, 2010.

Molotch, N. P.: Reconstructing snow water equivalent in the Rio Grande headwaters using remotely sensed snow cover data and a spatially distributed snowmelt model, Hydrol. Process., 23, 1076–1089, doi:10.1002/hyp.7206, 2009.

Molotch, N. P. and Bales, R. C.: Comparison of ground-based and airborne snow surface albedo parameterizations in an alpine watershed: impact on snowpack mass balance, Water Resour. Res., 42, W05410, doi:10.1029/2005WR004522, 2006.

Molotch, N. P. and Margulis, S. A.: Estimating the distribution of snow water equivalent using remotely sensed snow cover data and a spatially distributed snowmelt model: a multi-resolution, multi-sensor comparison, Adv. Water Resour., 31, 1503–1514, doi:10.1016/j.advwatres.2008.07.017, 2008.

Montgomery, D. R., Balco, G., and Willett, S. D.: Climate, tectonics, and the morphology of the Andes, Geology, 29, 579–582, 2001.

Neteler, M.: Estimating daily land surface temperatures in mountainous environments by reconstructed MODIS LST data, Remote Sens., 2, 333–351, doi:10.3390/rs1020333, 2010.

Neteler, M., Bowman, M. H., Landa, M., and Metz, M.: GRASS GIS: a multi-purpose open source GIS, Environ. Modell. Softw., 31, 124–130, 2012.

Newman, M., Compo, G. P., and Alexander, M. A.: ENSO-forced variability of the Pacific decadal oscillation, J. Climate, 16, 3853–3857, 2003.

Núñez, J., Rivera, D., Oyarzún, R., and Arumí, J. L.: Influence of Pacific Ocean multidecadal variability on the distributional properties of hydrological variables in north-central Chile, J. Hydrol., 501, 227–240, 2013.

Pomeroy, J. W., Marks, D., Link, T., Ellis, C., Hardy, J., Rowlands, A., and Granger, R.: The impact of coniferous forest temperature on incoming longwave radiation to melting snow, Hydrol. Process., 23, 2513–2525, doi:10.1002/hyp.7325, 2009.

Pontailler, J.-Y., Hymus, G. J., and Drake, B. G.: Estimation of leaf area index using ground-based remote sensed NDVI measurements: validation and comparison with two indirect techniques, Can. J. Remote Sens., 29, 381–387, 2003.

Ragettli, S., Cortés, G., McPhee, J., and Pellicciotti, F.: An evaluation of approaches for modelling hydrological processes in high-elevation, glacierized Andean watersheds, Hydrol. Process., 28, 5674–5695, doi:10.1002/hyp.10055, 2014.

Raleigh, M. S., Landry, C. C., Hayashi, M., Quinton, W. L., and Lundquist, J. D.: Approximating snow surface temperature from standard temperature and humidity data: new possibilities for snow model and remote sensing evaluation, Water Resour. Res., 49, 8053–8069, 2013.

Rankinen, K., Karvonen, T., and Butterfield, D.: A simple model for predicting soil temperature in snow-covered and seasonally frozen soil: model description and testing, Hydrol. Earth Syst. Sci., 8, 706–716, doi:10.5194/hess-8-706-2004, 2004.

Rhee, J. and Im, J.: Estimating high spatial resolution air temperature for regions with limited in situ data using MODIS products, Remote Sens., 6, 7360–7378, 2014.

Rittger, K., Painter, T. H., and Dozier, J.: Assessment of methods for mapping snow cover from MODIS, Adv. Water Resour., 51, 367–380, 2013.

Rubio-Álvarez, E. and McPhee, J.: Patterns of spatial and temporal variability in streamflow records in south central Chile in the period 1952–2003, Water Resour. Res., 46, W05514, doi:10.1029/2009WR007982, 2010.

Salazar, G. and Raichijk, C.: Evaluation of clear-sky conditions in high altitude sites, Renew. Energ., 64, 197–202, 2014.

Sicart, J. E., Essery, R. L., Pomeroy, J. W., Hardy, J., Link, T., and Marks, D.: A sensitivity study of daytime net radiation during snowmelt to forest canopy and atmospheric conditions, J. Hydrometeorol., 5, 774–784, 2004.

Slater, A. G., Barrett, A. P., Clark, M. P., Lundquist, J. D., and Raleigh, M. S.: Uncertainty in seasonal snow reconstruction: relative impacts of model forcing and image availability, Adv. Water Resour., 55, 165–177, doi:10.1016/j.advwatres.2012.07.006, 2013.

Tarboton, D. G. and Luce, C. H.: Utah Energy Balance Snow Accumulation and Melt Model (UEB), Citeseer, Utah Water Research Laboratory, p. 63, 1996.

Vera, C., Silvestri, G., Liebmann, B., and González, P.: Climate change scenarios for seasonal precipitation in South America from IPCC-AR4 models, Geophys. Res. Lett., 33, L13707, doi:10.1029/2006GL025759, 2006.

Vicuña, S., Garreaud, R. D., and McPhee, J.: Climate change impacts on the hydrology of a snowmelt driven basin in semiarid Chile, Clim. Change, 105, 469–488, doi:10.1007/s10584-010-9888-4, 2011.

Wan, Z., Zhang, Y., Zhang, Q., and Li, Z.: Validation of the land-surface temperature products retrieved from Terra Moderate Resolution Imaging Spectroradiometer data, Remote Sens. Environ., 83, 163–180, 2002.

Wan, Z., Zhang, Y., Zhang, Q., and Li, Z.-L.: Quality assessment and validation of the MODIS global land surface temperature, Int. J. Remote Sens., 25, 261–274, 2004.

Williamson, S. N., Hik, D. S., Gamon, J. A., Kavanaugh, J. L., and Flowers, G. E.: Estimating temperature fields from MODIS land surface temperature and air temperature observations in a sub-Arctic Alpine environment, Remote Sens., 6, 946–963, 2014.

Table 1. Study area subdivision, relevant characteristics and model parameters.

Cluster	Area × 10^3 [km^2]	Average elevation [m a.s.l.]	Average cluster latitude [°]	Clear sky Index (K_c)	Avg. a_r [$cm\,^{\circ}C^{-1}\,day^{-1}$]	T_a [°C]	Forest Cover [%]
C1	26.5	3300	−29.4	0.78	0.02	18.3	2.0
C2	17.9	2760	−33.7	0.89	0.11	16.1	5.5
C3	9.20	1890	−36.4	0.83	0.18	12.2	13.8
C4	49.3	3520	−30.1	0.8	0.04	20.4	1.4
C5	18.5	2855	−33.4	0.83	0.15	15.6	3.0
C6	7.60	2807	−34.8	0.83	0.21	13.9	2.3
C7	14.8	2167	−36.1	0.85	0.20	16.7	2.5
C8	8.30	1840	−37.0	0.82	0.23	15.7	4.9
Total/Average	152.1	2320	***	0.83	0.14	***	3.3

Title Page

Abstract Introduction

Conclusions References

Tables Figures

◀I ▶I

◀ ▶

Back Close

Full Screen / Esc

Printer-friendly Version

Interactive Discussion

Table 2. Snow pillow (SP) measurements available within the study domain.

ID	SWE data	Symbol	Lat. (S)	Long. (W)	Elevation [m a.s.l.]
CHILE					
1	Quebrada Larga	QUE	30°43’	70°16’	3500
2	Cerro Vega Negra	CVN	30°54’	70°30’	3600
3	El Soldado	SOL	32°00’	70°19’	3290
4	Portillo	POR	32°50’	70°06’	3000
5	Laguna Negra	LAG	33°39’	70°06’	2780
6	Lo Aguirre	LOA	35°58’	70°34’	2000
7	Alto Mallines	ALT	37°09’	70°14’	1770
ARGENTINA					
8	Toscas	TOS	33°09’	69°53’	3000
9	Laguna Diamante	DIA	34°11’	69°41’	3300
10	Laguna Atuel	ATU	34°30’	70°02’	3420
11	Valle Hermoso	VAL	35°08’	70°12’	2250
12	Paso Pehuenches	PEH	35°08’	70°23’	2545

Table 3. Summary of snow depth and density intensive study campaigns.

Year	ID (Fig. 1)	Symbol	Field site	Date	Snow-pit density [$\mathrm{kg\,m^{-3}}$]	SWE average [mm]	SWE std. dev. [mm]	SWE range [mm]	Sample size
2010	2	ODA	Ojos de Agua	25 Sep	352	450	163	848–0	134
2011	2	ODA	Ojos de Agua	30 Aug	341	705	199	1194–136	374
	5	MOR	Morales	1 Sep	367	642	282	1101–0	171
	8	OBL	Olla Blanca DET	31 Aug	333	539	217	1032–79	289
2012	1	CVN	Cerro Vega Negra	28 Aug	308	296	115	700–40	166
	3	MAR	Juncal–Mardones	30 Aug	373	530	230	1120–40	163
	5	MOR	Morales	12 Sep	412	590	360	1240–150	152
	8	OBL	Olla Blanca DET	3 Sep	411	590	260	1230–0	309
	4	POR	Portillo	15 Sep	410	170	180	1230–0	181
2013	1	CVN	Cerro Vega Negra	21 Aug	356	405	165	1040–10	282
	2	ODA	Ojos de Agua	23 Aug	355	540	220	1310–100	300
	10	CHI	Nevados Chillán[a]	27 Aug	416	980	240	1270–30	104
	10	CHI	Nevados Chillán[b]	27 Aug	416	600	240	1230–70	216
	4	POR	Portillo	23 Aug	392	340	210	1120–0	91
	6	LAG	Laguna Negra	30 Aug	455	480	250	1770–0	32
2014	1	CVN	Cerro Vega Negra	5 Aug	321	163	85	620–0	326
	5	MOR	Morales	12 Aug	401	510	250	1190–0	329
	7	LVD	Lo Valdez	13 Aug	365	710	290	1260–0	186
	8	OBL	Olla Blanca DET	12 Sep	363	420	240	1210–0	334
	9	RBL	Río Blanco DET	6 Sep	354	620	290	1210–0	99
	10	CHI	Nevados Chillán[a]	26 Sep	504	830	400	380–1510	18
	10	CHI	Nevados Chillán[b]	26 Sep	504	980	250	530–1500	87
	4	POR	Portillo	19 Aug	436	170	140	850–0	73
	6	LAG	Laguna Negra	30 Aug	365	300	110	540–0	117

[a] Without forest cover (upper part of basin).
[b] With forest cover (lower part of basin).

Table 4. Model validation statistics against intensive study area observations around snow pillows and at catchment scale.

Reconstructed SWE vs. MODIS pixel (grid) sampling (selected snow-pillows)

	Avg. Sampling [mm] (1)	SD Sampling [mm] (2)	Avg. Model [mm] (3)	SP (sensor) [mm] (4)	RE$_{\%}$ (avg.) (1) vs. (3)	RE$_{\%}$ (avg.) (1) vs. (4)	RE$_{\%}$ (avg.) (3) vs. (4)
CVN	223	110	334	200	49 %	−10 %	98 %
POR	227	177	170	353	−25 %	35 %	−51 %
LAG	395	180	283	280	−28 %	−30 %	8 %

Reconstructed SWE vs. snow surveys (pilot-basins)

	Avg. Sampling [mm] (1)	SD Sampling [mm] (2)	avg. Model [mm] (3)	SD Model [mm] (4)	RE$_{\%}$ (avg.) (1) vs. (3)	RE$_{\%}$ (SD) (2) vs. (4)
CVN	253	133	298	63	18 %	−53 %
ODA-MAR	556	203	535	128	−4 %	−37 %
MOR-LVD	613	295	375	115	−39 %	−61 %
OBL-RBL	497	252	317	89	−36 %	−65 %
CHI (forest)	790	245	257	46	−67 %	−81 %
CHI (clear)	905	320	724	170	−20 %	−47 %

Reconstructed SWE vs. snow -pillows (1 Sep – Chile and 1 Oct – Argentina)

	R^2	SE$_{\bar{x}}$ [mm]	RE$_{\%}$	RMSE [mm]	Mod. SWE average [mm]	Mod. SWE SD [mm]
QUE	0.71	208	79	335	529	350
CVN	0.78	140	56	251	609	281
SOL	0.68	112	−19	127	401	241
POR	0.32	277	−36	398	437	324
LAG	0.42	217	−21	230	424	263
LOA	0.88	123	−5	171	734	316
ALT	0.83	89	−41	332	489	296
TOS	0.78	72	−52	251	120	141
DIA	0.76	141	−4	137	455	291
ATU	0.56	378	9	349	1263	496
VAL	0.72	211	−24	273	457	371
PEH	0.74	334	32	436	1302	580
Average	0.68	192	−2	274	602	330

Table 5. Peak SWE 2001–2014 climatology for river basins within the study region. Basin-wide averages, SCA-wide averages and basin-wide water volumes shown.

ID	Basin-gauge station	Lat. S	Long. W	Outlet Elev. [m a.s.l.]	Area [km^2]	SWE		
						Basin-wide [mm]	Over-SCA [mm]	Basin-wide [m^3 × 10^{-6}]
	CHILE							
1	Copiapó en Pastillo	27°59’	69°58’	1300	7470	45	120	336
2	Huasco en Algodones	28°43’	70°30’	750	7180	68	161	488
3	Elqui en Algarrobal	29°59’	70°35’	760	5710	151	269	862
4	Hurtado en San Agustín	30°27’	70°32’	2050	676	302	325	204
5	Grande en Puntilla San Juan	30°41’	70°55’	2140	3545	137	306	486
6	Cogotí en La Fraguita	31°06’	70°53’	1021	491	182	335	89
7	Illapel en Huintil	31°33’	70°57’	650	1046	180	305	188
8	Chalinga en San Agustín	31°41’	70°43’	920	437	142	332	62
9	Choapa en Salamanca	31°48’	70°55’	560	2212	214	356	473
10	Sobrante en Picadero	32°12’	70°42’	2057	126	172	198	22
11	Alicahuen en Colliguay	32°18’	70°44’	852	344	92	184	32
12	Putaendo en Resg. Los Patos	32°30’	70°34’	1218	890	273	346	243
13	Aconcagua en Chacabuquito	32°51’	70°30’	950	2110	609	692	1285
14	Mapocho en Los Almendros	33°22’	70°27’	970	640	269	342	172
15	Maipo en El Manzano	33°35’	70°22’	850	4840	692	760	3349
16	Cachapoal en Puente Termas	34°15’	70°34’	700	2455	700	814	1719
17	Tinguiririca en Los Briones	34°43’	70°49’	560	1785	532	677	950
18	Teno en Claro	34°59’	70°49’	650	1210	438	524	530
19	Lontué en Colorado–Palos	35°15’	71°02’	600	1330	656	759	872
20	Maule en Armerillo	35°42’	70°10’	470	5465	525	554	2869
21	Ñuble en San Fabián	36°34’	71°33’	410	1660	376	430	624
22	Polcura en Laja	37°19’	77°32’	675	2088	358	378	748
	ARGENTINA							
23	Jachal en Pachimoco	30°12’	68°49’	1563	24 266	79	175	1917
24	San Juan en km 101	31°15’	69°10’	1129	23 860	308	569	7349
25	Mendoza en Guido	32°54’	69°14’	1479	7304	460	672	3360
26	Tunuyán en Zapata	33°46’	69°16’	852	11 230	289	592	3245
27	Diamante en La Jaula	34°40’	69°18’	1451	19 332	395	489	7636
28	Atuel en Loma Negra	35°15’	69°14’	1353	3696	338	525	1249
39	Malargue en La Barda	35°33’	69°40’	1568	1055	171	284	180
30	Colorado en Buta Ranquil	37°04’	69°44’	817	14 896	288	495	4290
31	Neuquén en Rahueco	37°21’	70°27’	870	8266	356	446	2943

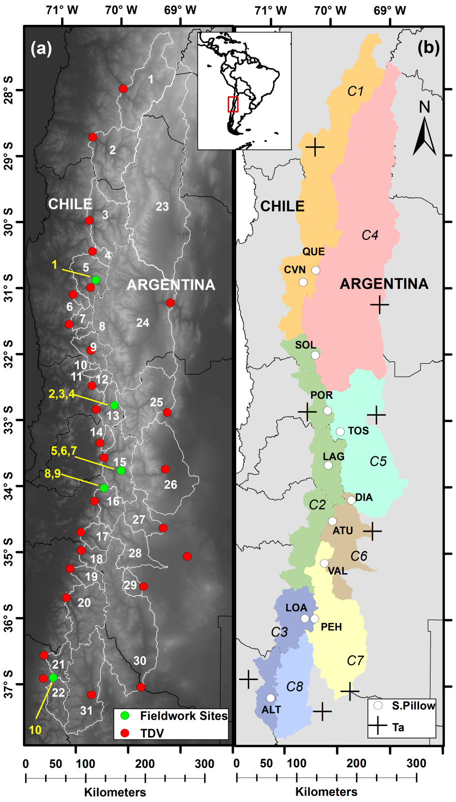

Figure 1. Study area and model domain: **(a)** river basins, stream gages (red circles) and sites where snow survey data are available (green circles), **(b)** hydrologic units (C1 to C8) and snow-pillow stations (white circles).

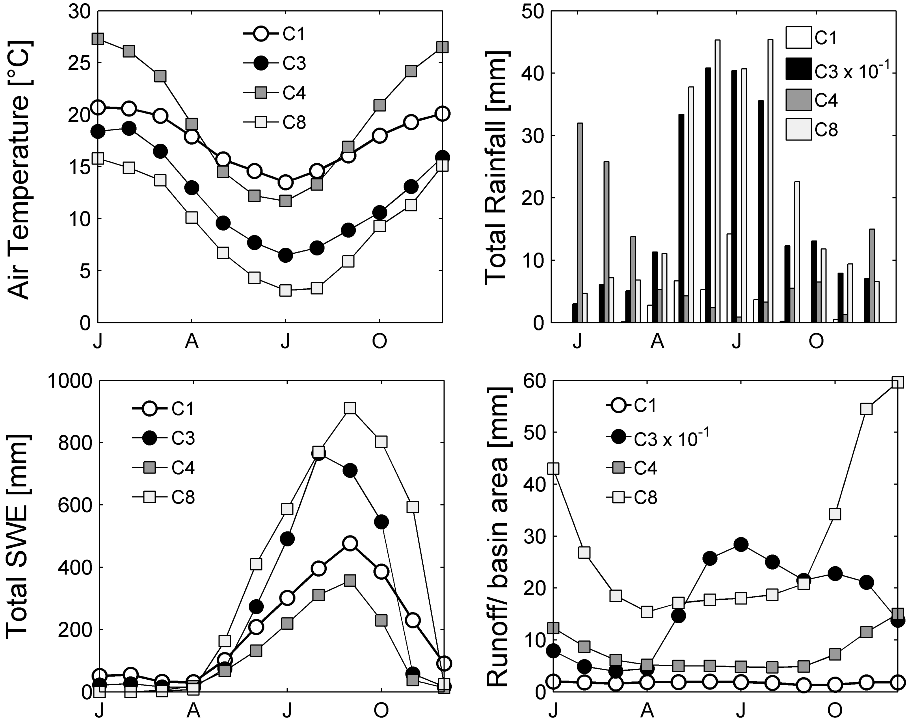

Figure 2. Summarized hydroclimatology of the model domain. Data from meteorological stations located within zones C1, C4, C3 and C8 summarized the hidro-climatology regime of northern-west, northern-east, southern-west and southern-east zones respectively.

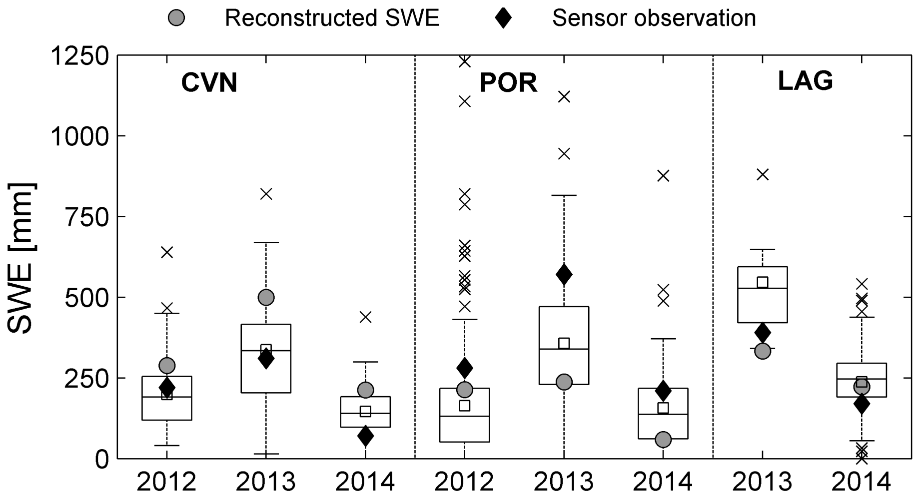

Figure 3. Reconstructed SWE validation at selected snow-pillow sites. Black diamonds are instrumental records, gray circles are model estimates, and box-plots summarize manual verification dataset around the pillow site. Upper and lower box limits are the 75 and 25 % quartiles, horizontal line is the median, white box is the mean, upper and lower dashes represent plus and minus 2.5 standard deviations from the mean, and crosses are outlying values.

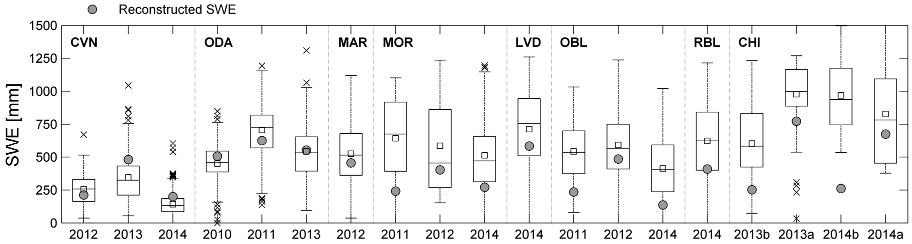

Figure 4. Reconstructed SWE validation at pixels with snow survey data. Box plots summarize all individual measurements at pixels co-located with SWE reconstruction. Symbology analogous to Fig. 3.

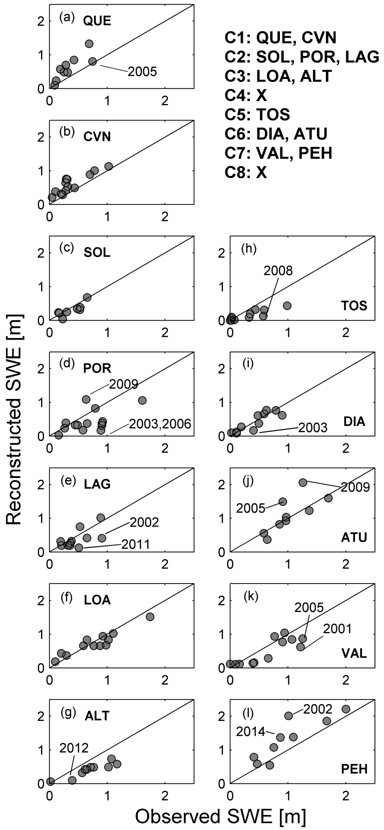

Figure 5. Comparison between peak reconstructed and observed SWE at snow-pillow sites. Solid line represents the 1 : 1 line.

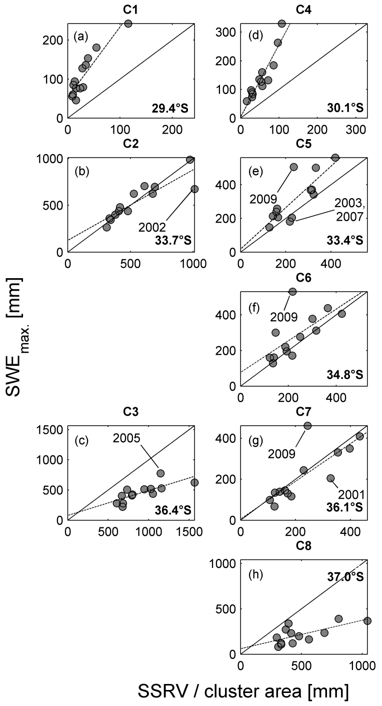

Figure 6. Area-specific spring–summer runoff volume (SSRV) vs. peak SWE. Clusters 1 through 3 include rivers on the Chilean (western) slope of the Andes range; clusters 4 through 8 correspond to Argentinean (eastern) rivers. Solid line represents 1 : 1 line. C4 and C8 SSRV were estimated by area-transpose method.

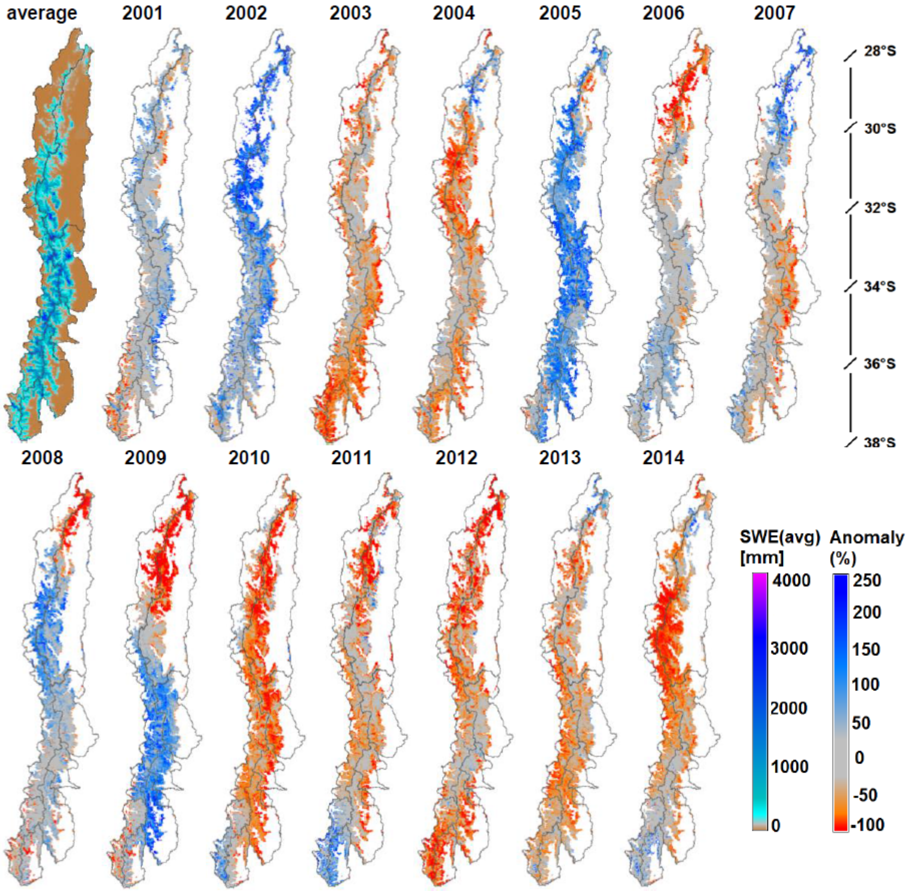

Figure 7. Regional peak (1 September) SWE Climatology for the 2001–2014 period (upper left panel), and annual peak SWE anomalies.

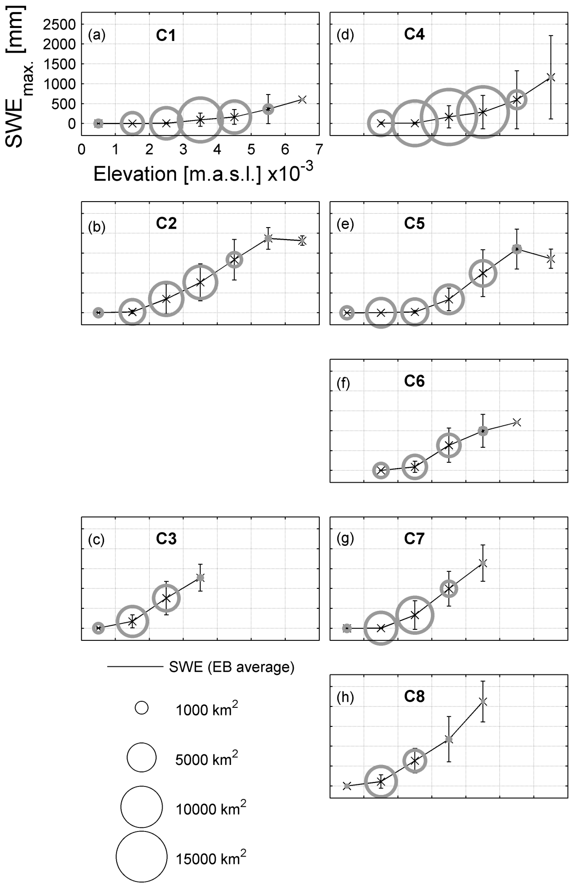

Figure 8. Maximum SWE through 1000 m elevation bands (EB). Crosses are mean values within EB, lines are estimated SWE-elevation profile. Circle radius indicate EB area [km^2] scaled by 0.05 and takes values from SWE axis.

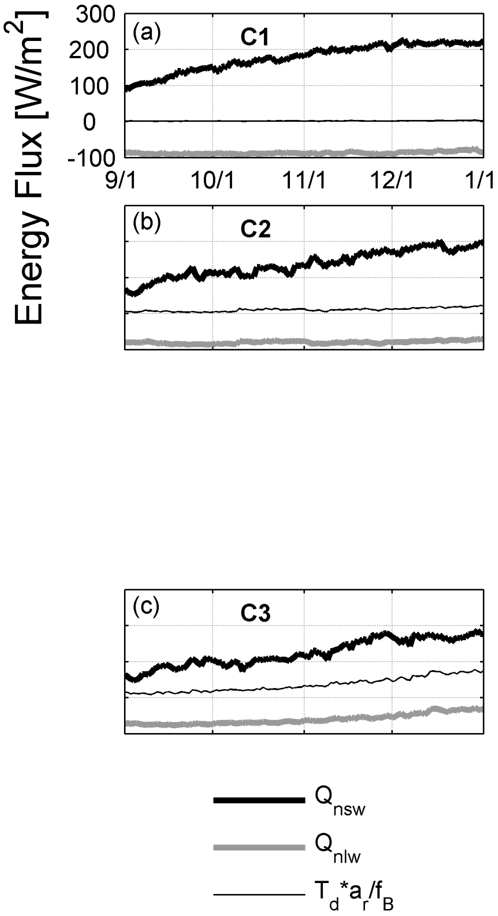

Figure 9. Time series of energy fluxes over snow surface (average over 14 years) and global average per cluster. Unique axes scale for all plots.

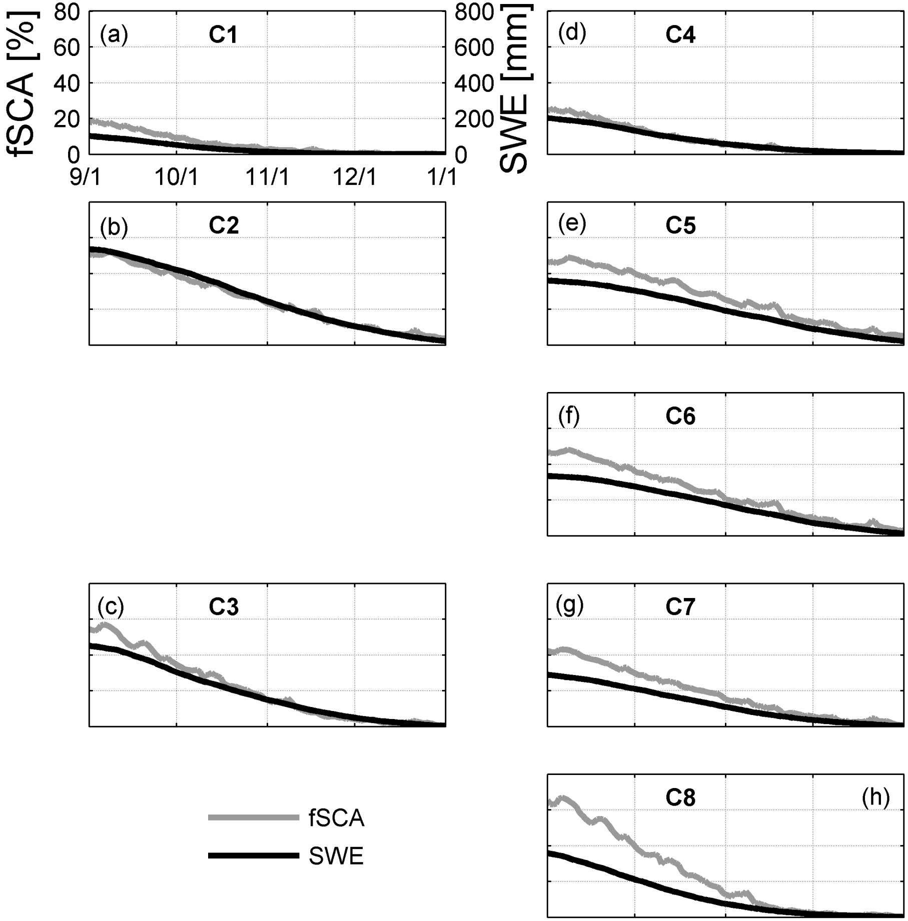

Figure 10. Average seasonal evolution of fSCA and SWE in the study region. Lower right panel shows the spatial correlation between time-averaged fSCA, SWE and specific melt-season river discharge.

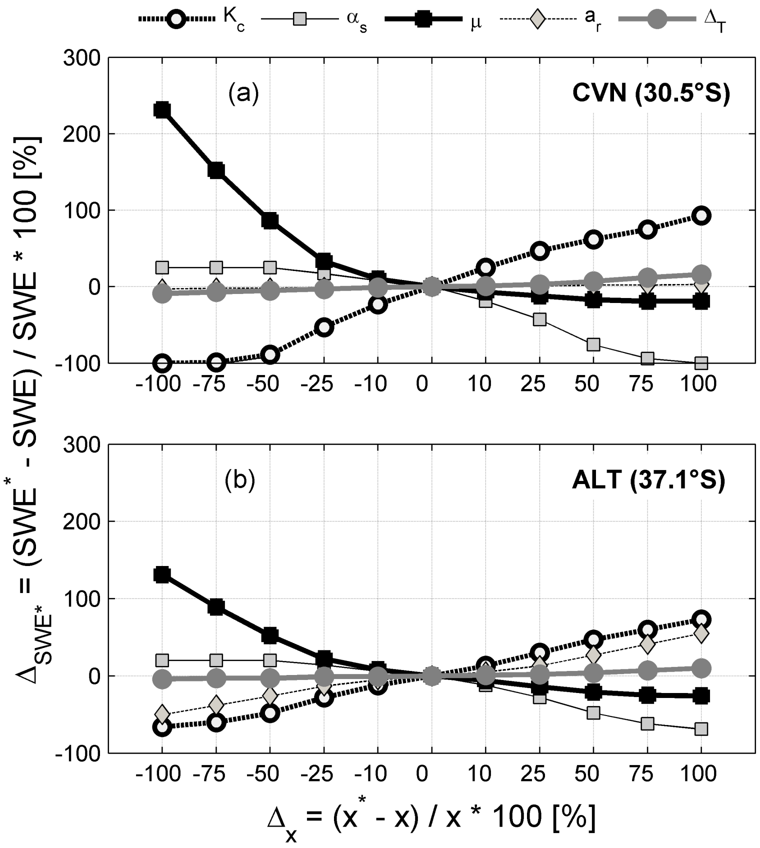

Figure 11. Sensitivity of peak SWE estimates to model forcings and parameters. Average over the 2001–2014 period at selected snow pillow sites. Δ_x represents the percentage change over each parameter studied respect to the base case.

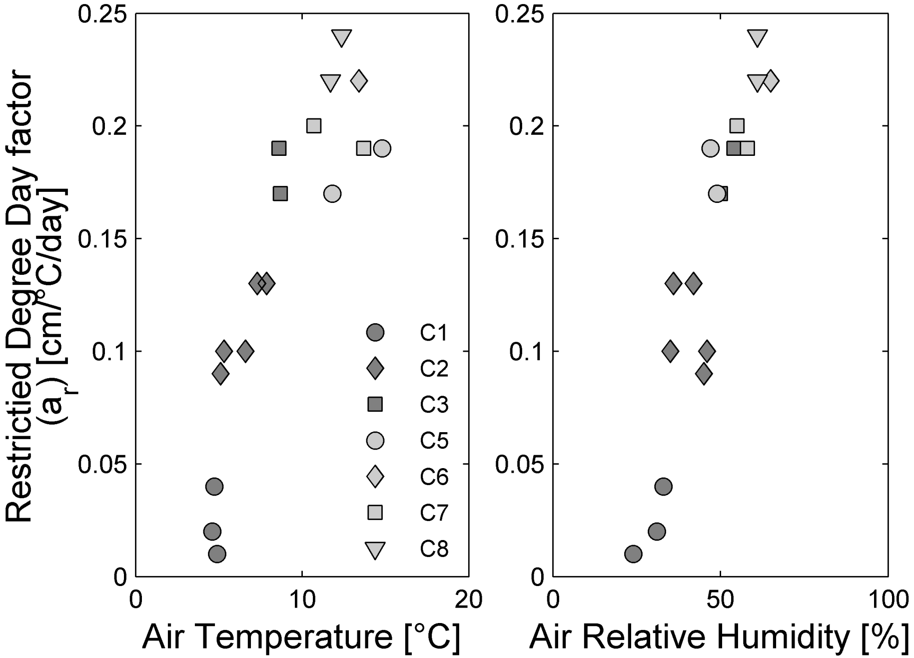

Figure 12. Restricted Degree Day factor as a function of space (basin cluster) and climatological properties.